Environmental Science: Atmospheres

ROYAL SOCIETY OF CHEMISTRY

PAPER

View Article Online
View Journal

Cite this: DOI: 10.1039/d6ea00030d

Optical properties of prebiotic seawater analogs and sea-spray aerosols

Mae K. A. Johnson,[a] Alexander Logozzo,[b] Aaron M. Palmisano,[c] Vahid Shahabadi,[a] James F. Davies [c] and Thomas C. Preston *[ab]

Optical constants for plausible Hadean seawater and seawater-derived marine aerosols are needed to constrain early Earth radiative transfer and surface photochemistry, yet they remain poorly characterized. Here we report the wavelength-, temperature-, and water-activity-dependent complex refractive index, $m(\lambda) = n(\lambda) + ik(\lambda)$, for modern seawater and three model prebiotic seawater compositions chosen to represent the leading hypotheses for primordial ocean chemistry, including sulfate-depleted, chloride-dominated analogs and a Ca-enriched, crust-controlled analog. Using single-particle measurements *via* optical trapping (OT) and an electrodynamic balance (EDB), we retrieve n and quantify weak visible absorption (k on the order of 10^{-9}) across water activities relevant to concentrated sea-spray aerosol and near-surface waters. Complementary bulk refractometry extends the dataset to high water activity and provides the temperature dependence of n from 10–70 °C. The measurements are consistent with an effective-oscillator description for weakly absorbing aqueous aerosols. EDB measurements additionally confirm that the three prebiotic solutions exhibit similar hygroscopic growth, supporting their use as controlled analogs for seawater-derived aerosol particles. Together, these results provide physically grounded inputs for paleoclimate radiative-transfer calculations and for representing the optical impacts of marine aerosols generated from hypothesized early Earth seawater.

Received 26th February 2026
Accepted 29th March 2026

DOI: 10.1039/d6ea00030d

rsc.li/esatmospheres

Environmental significance

Sea-spray aerosol is Earth's largest natural particulate source and strongly influences radiation, clouds, and heterogeneous chemistry. Yet optical property data for seawater-derived particles are almost entirely limited to modern seawater, despite evidence that Archean oceans may have had markedly different ionic compositions. We provide single-particle measurements of hygroscopic growth and complex refractive index for three plausible prebiotic seawater analogs and compare them to modern seawater. These measurements constrain physically consistent, wavelength-resolved $n(\lambda)$ and $k(\lambda)$ needed for radiative-transfer and photochemical models. The resulting dataset reduces a key uncertainty in simulations of early Earth climate and supports interpretation of aerosol and ocean signatures on Earth-like exoplanets.

1 Introduction

A key challenge in origin-of-life research is to constrain the range of environmental conditions on early Earth under which prebiotic chemistry could plausibly proceed. This is especially difficult for the Hadean Earth because the geologic record is sparse and direct samples are unavailable, leaving substantial uncertainty in surface conditions and ocean composition.[1,2] These uncertainties propagate into models for surface photochemistry and into climate calculations for an Earth receiving less solar luminosity than today (the faint young Sun problem).[3,4]

Light is relevant to early Earth habitability in at least two interrelated ways. First, solar radiation provides an energy source for prebiotic photochemistry and photocatalysis, motivating quantitative constraints on the spectral photon flux at the surface and within plausible aqueous environments.[5] Second, solar radiation dominates the surface energy budget, so the partitioning of light among atmospheric absorption, scattering, and ocean uptake directly influences inferred climate states.[4] In both cases, translating boundary-condition assumptions into quantitative radiative-transfer predictions requires optical properties for the participating media, including the complex refractive index of seawater and seawater-derived aerosol particles. The complex refractive index, $m(\lambda) = n(\lambda) + ik(\lambda)$, controls Fresnel reflection at the air–sea interface, refraction and focusing within droplets, and the scattering and absorption efficiencies that govern radiative impacts and light penetration depth.

[a]Department of Atmospheric and Oceanic Sciences, McGill University, Montreal, QC, H3A 0B9, Canada. E-mail: thomas.preston@mcgill.ca
[b]Department of Chemistry, McGill University, Montreal, QC, H3A 0B8, Canada
[c]Department of Chemistry, University of California Riverside, CA, 92521, USA

Marine aerosols provide an additional pathway by which seawater composition can influence both climate and aqueous photochemistry. Sea-spray aerosol (SSA) is generated by bubble bursting and wave breaking and is a major contributor to the atmospheric aerosol burden over the oceans.[6,7] Fresh SSA efficiently scatters solar radiation and can act as cloud condensation nuclei, linking its physicochemical and optical properties to Earth's radiative balance.[8] Because SSA originates from seawater, its composition and hygroscopic growth depend on seawater ion ratios and other constituents, and its optical properties depend on both composition and relative humidity.[6,8] Parameterizations commonly used for present-day marine aerosols[9,10] are not guaranteed to apply to a prebiotic ocean whose ionic makeup may have differed substantially from modern seawater.

A central uncertainty is therefore the composition of Hadean and early Archean seawater. Multiple lines of evidence and modeling suggest that sulfate concentrations in the Archean ocean were far lower than modern values because oxidative weathering and the oxidative sulfur cycle were limited under low atmospheric oxygen.[11–13] A common approximation is thus to treat prebiotic seawater as modern major-cation abundances with sulfate removed and chloride as the dominant counterion.[14,15] An alternative perspective emphasizes strong water–rock interaction during ocean formation and evolution, potentially yielding seawater with substantially different cation ratios, including elevated Ca^{2+} relative to modern seawater.[16] Beyond sulfate, reconstructions of Archean seawater salinity and major-ion chemistry remain debated, with constraints drawn from fluid inclusions and halide systematics in Archean crustal and hydrothermal records and from broader geochemical reconstructions of seawater evolution through time.[17–27] Sedimentary archives (for example evaporites) and modeling studies further indicate that plausible ranges in salinity and seawater composition can be climatically and chemically consequential.[28–31] These distinct compositional scenarios motivate systematic measurements on model solutions representing both sulfate-depleted, modern-like and crust-controlled ocean chemistry.

For modern seawater, the real refractive index is sufficiently well characterized that empirical formulas exist across wavelength, temperature, and salinity.[32–37] Additionally, some parameterizations also include pressure.[32] Comparable data are scarce for prebiotic seawater analogs, particularly for (i) wavelength-dependent dispersion for proposed early ocean ion ratios, (ii) the metastable and supersaturated regime relevant to aerosol droplets and evaporating surface microlayers, and (iii) the imaginary component $k(\lambda)$ that determines absorption and therefore light penetration depths. Even when absorption is weak in the visible, small differences in k can matter for photochemical action spectra and for separating scattering from absorption in radiative-transfer calculations.[38]

Here we report wavelength- and temperature-dependent complex refractive indices for modern seawater and three model prebiotic seawater solutions chosen to represent the principal compositional hypotheses discussed above.[14,16] We combine bulk refractometry at high water activity with single-particle measurements to retrieve n and k over a wide range of water activities relevant to both ocean surface waters and humidified marine aerosols. Finally, we compare our results to existing seawater and sea-spray aerosol refractive-index parameterizations and measurements, and discuss the implications for representing seawater-derived aerosol optics in prebiotic scenarios.

2 Experimental section

2.1 Preparation of model prebiotic seawater solutions

Three model prebiotic seawater solutions (SW1, SW2, and SW3) were prepared to span leading hypotheses for primordial ocean major-ion chemistry. SW1 and SW3 follow a sulfate-depletion approach in which sulfate in modern seawater is removed and chloride provides charge balance while maintaining modern-like major cation ratios.[14,39] This composition reflects expectations that low atmospheric oxygen limited oxidative weathering and sulfate delivery to the ocean.[15,40] SW2 is based on compositions inferred from crust–water interaction experiments intended to simulate early ocean formation, which yield a Ca-enriched dissolved ion distribution.[14,16,41] Additionally, modern seawater (MSW) was prepared as a present-day reference composition to benchmark the prebiotic solutions and enable direct comparison with established seawater and sea-salt aerosol literature. Preparation of MSW followed ASTM D1141-98 substitute ocean water, but included only the five major salts (NaCl, $MgCl_2$, Na_2SO_4, $CaCl_2$, and KCl).[42] Ion mole fractions used to define each solution are reported in Table 1. Minor ions beyond Na^+, K^+, Mg^{2+}, Ca^{2+}, Cl^-, and SO_4^{2-} were neglected.

Sodium chloride (NaCl, ACS reagent, ≥99.0%, Sigma-Aldrich), potassium chloride (KCl, ≥99.0%, Sigma-Aldrich), magnesium chloride ($MgCl_2$, anhydrous, ≥98%, Sigma-Aldrich), calcium chloride ($CaCl_2$, anhydrous, ≥93.0%, Sigma-Aldrich), and sodium sulfate (Na_2SO_4, ACS reagent, anhydrous, ≥99.0%, Sigma-Aldrich) were purchased commercially and used as received. All solutions were prepared using deionized water.

For each seawater formulation (SW1, SW2, SW3, and MSW), the required salt masses were calculated from the target ion mole fractions (Table 1) using the salt stoichiometries, with chloride salts supplying the major ions (Na^+, K^+, Mg^{2+}, Ca^{2+}) and

Table 1 Ion mole fractions for the model prebiotic seawaters and modern seawater. SW1 and SW3 follow sulfate-to-chloride replacement formulations,[14,39] whereas SW2 is based on a Ca-enriched composition derived from crust–water interaction studies.[16] MSW is based on the ASTM D1141-98 substitute ocean water formulation, using only the five major salts (NaCl, $MgCl_2$, Na_2SO_4, $CaCl_2$, and KCl)[42]

	SW1	SW2	SW3	MSW
Na^+	0.409	0.0865	0.407	0.419
K^+	0.00865	0.00370	0.00905	0.00818
Mg^{2+}	0.0463	0.0775	0.0471	0.0479
Ca^{2+}	0.00865	0.196	0.00878	0.00917
Cl^-	0.527	0.637	0.528	0.491
SO_4^{2-}	0	0	0	0.0253

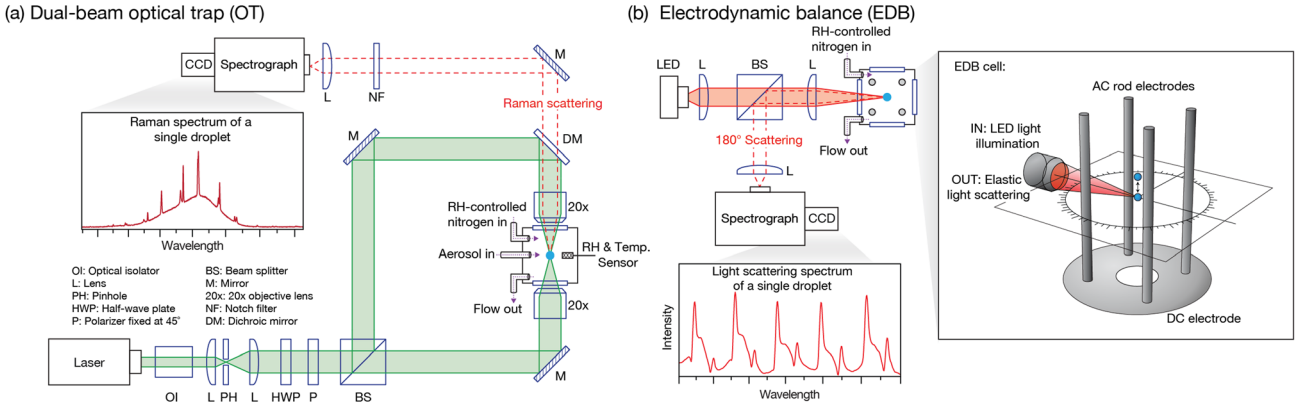

Fig. 1 Schematics of the experimental platforms used in this study. (a) Dual-beam optical trap (OT) with cavity-enhanced Raman spectroscopy for single-particle complex refractive index measurements. (b) Linear quadrupole electrodynamic balance (EDB) for hygroscopic growth and real part of the refractive index measurements.

Cl^-. Salts were weighed gravimetrically on an analytical balance into pre-cleaned containers, dissolved in deionized water with gentle stirring until homogeneous. Solutions were prepared at high concentration (typically near saturation) to support trapping of larger droplets, and were diluted gravimetrically as needed for bulk measurements. Prepared solutions were stored in the dark in airtight containers to minimize evaporation.

2.2 Single-particle measurement of complex refractive index in an optical trap

The experiments used a dual-beam optical trap (OT), described previously.[43,44] A schematic is shown in Fig. 1a. Trapping was performed using 532 nm light from a diode-pumped solid-state laser (Opus 532, Laser Quantum). The beam was passed through a half-wave plate (HWP) and a 3.3× Keplerian beam expander that slightly underfilled the back-aperture of the objectives, with a 35 μm pinhole placed at the overlapping focal points of the two expander lenses. The expanded beam was split into two equal-power, counter-propagating arms using a polarizing beam splitter (PBS). The polarizer orientation was adjusted to balance the power in each arm, which was verified using two photodiodes (SM1PD1A, Thorlabs). Each arm was focused using opposing 20× long-working-distance microscope objectives (Plan APO ELWD 20×, Motic) whose focal points overlapped at the trapping position inside a custom, temperature-regulated trapping cell.

Aerosol droplets were generated using a medical nebulizer (TurboBOY SX, PARI) and introduced directly into the uppermost module of the trapping cell. Relative humidity (RH) was controlled by adjusting the ratio of wet and dry nitrogen to a fixed total flow (typically 100 sccm) using mass flow controllers, and RH and temperature were monitored using a capacitive RH/T sensor (SHT75, Sensirion) positioned ~10 mm from the trapped particle. All measurements were performed at 23 ± 1 °C. This is also the temperature used for all subsequent calculations.

Cavity-enhanced Raman spectroscopy (CERS) spectra were collected by passing the backscattered light through a notch filter (NFD01-532, Semrock) and directing it into a grating spectrograph (IsoPlane SCT-320, Princeton Instruments) equipped with a CCD detector (PIXIS:100B_eXcelon, Princeton Instruments). The spectra contain the water OH-stretch band with superimposed morphology-dependent resonances (MDRs). The MDR peak positions were extracted and fit using Mie theory (MRFIT) to retrieve the droplet radius and refractive index.[45,46]

For each solution, a droplet was trapped near the maximum accessible humidity (approximately 80% RH) and RH was then decreased stepwise (2% increments) until efflorescence occurred (typically 35–50% RH depending on composition). To reduce laser-induced heating and associated shifts in droplet composition, the trapping laser power was set to 500 mW at higher RH and reduced to 150 mW at lower RH. Note that for the micron-sized droplets studied here, the Kelvin effect is negligible ($\Delta a_w \lesssim 10^{-4}$ for $r \gtrsim 1$ μm), and we therefore approximate the droplet water activity in the trap as $a_w \approx$ RH/100%.

The imaginary part of the refractive index, k, was measured only at the trapping-laser wavelength ($\lambda = 532$ nm), following the methodology described in ref. 43 and 47. In brief, the trapping laser power was varied over 200–300 mW during each measurement, while the RH was held constant. The RH was then decreased stepwise (4% increments) from approximately 80%, with four replicate measurements at each RH. For each RH step, the radius and n were determined by MRFIT and subsequently processed to extract k(532 nm).

Although k is measured at a single wavelength (532 nm here), the wavelength-dependent absorption spectrum, $k(\lambda)$, can be obtained by enforcing Kramers–Kronig consistency between $n(\lambda)$ and $k(\lambda)$ using the effective oscillator framework of Bain and Preston.[47] In this approach it is convenient to work in wavenumber $\nu = 1/\lambda$, and the complex refractive index of a weakly absorbing aqueous solution is parameterized as

$$n(\nu) = 1 + \phi_s \frac{2}{\pi} \frac{\tilde{B}\tilde{\nu}_0}{\tilde{\nu}_0^{\,2} - \nu^2} + \phi_w \left(n^{(w)}(\nu) - 1\right), \quad (1)$$

$$k(\nu) = \phi_s \frac{2\nu}{\pi} \frac{\tilde{B}\tilde{\nu}_0\tilde{\Gamma}}{\left(\tilde{\nu}_0^2 - \nu^2\right)^2} + \phi_w k^{(w)}(\nu), \quad (2)$$

where ϕ_s and ϕ_w are the solute and water volume fractions, $n^{(w)}(\nu)$ and $k^{(w)}(\nu)$ are the real and imaginary parts of the refractive index of pure water, and $\tilde{B}$, $\tilde{\nu}_0$, and $\tilde{\Gamma}$ are effective oscillator parameters.[47] The volume fractions ϕ_s and ϕ_w are determined from the measured hygroscopic growth, as described in Section 2.4. The measured dispersion of $n(\lambda)$ constrains $\tilde{B}$ and $\tilde{\nu}_0$, while the measured k at 532 nm provides the remaining constraint needed to determine $\tilde{\Gamma}$, yielding continuous, Kramers–Kronig-consistent expressions for both $n(\lambda)$ and $k(\lambda)$ across the wavelength range relevant to the calculations reported below. In this framework, the multicomponent sea-salt mixtures examined here are treated as a single effective solute, such that ϕ_s represents the total dry solute volume fraction and $\tilde{B}$, $\tilde{\nu}_0$, and $\tilde{\Gamma}$ should be interpreted as mixture-averaged (effective) oscillator parameters.

The pure-water contributions $n^{(w)}(\nu)$ and $k^{(w)}(\nu)$ were taken from literature optical constants: $n^{(w)}(\nu)$ was calculated using the temperature- and wavelength-dependent parameterization of Harvey *et al.*,[48] while $k^{(w)}(\nu)$ was obtained by interpolation of the tabulated pure-water data compiled by Segelstein.[49]

2.3 Bulk refractometry at high water activity and variable temperature

Bulk refractometer measurements were used to extend the n dataset to high water activity, where the optical trap cannot access sufficiently dilute compositions. For each system, a saturated stock solution was prepared and diluted to generate a series of ten solutions spanning 10% to 100% of the saturated concentration. Water activity was measured using a water activity meter (AquaLab 4 TE, METER Group, Inc.), and n was measured with an Abbe refractometer. These measurements provide overlap with the high-a_w end of the single-particle dataset and extend toward pure water, typically spanning $a_w \approx 0.80$–0.99.

Temperature dependence was measured for the bulk dilution series by circulating temperature-controlled water through the refractometer. Measurements were performed from 10 °C to 70 °C in 5 °C increments, with triplicate measurements at each temperature. This temperature range overlaps estimates for early ocean surface temperatures.[50]

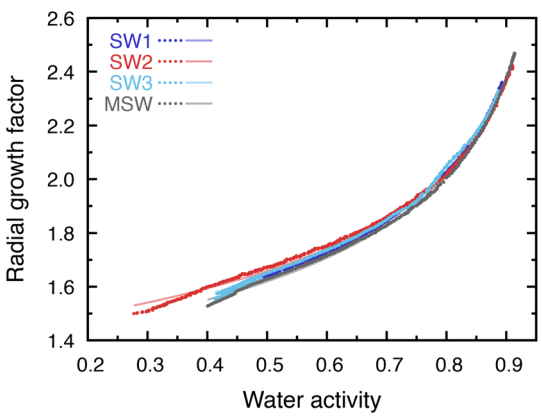

Fig. 2 Radial growth factor as a function of water activity for three model prebiotic seawater solutions (SW1–SW3) and modern seawater (MSW). Electrodynamic balance (EDB) measurements are shown as points. Solid lines show best-fits using eqn (4). Parameters of best-fit are listed in Table 2.

2.4 Hygroscopic growth and refractive index measurements in an electrodynamic balance

Hygroscopic growth and the real part of the refractive index, n, were measured using a linear quadrupole electrodynamic balance (EDB) operated under controlled environmental conditions.[51] A schematic is shown in Fig. 1b. Micron-sized aqueous droplets were generated using a piezoelectric droplet dispenser (Microfab MJ-ABP-01) driven by an in-house voltage pulser, and were charged by induction during generation using an electrode held at +200 to +500 V. Charged droplets were confined along the rod axis of the EDB and stabilized above a balancing DC electrode. A proportional–integral–derivative (PID) feedback loop was used to regulate the balancing voltage and maintain droplet position. Droplets were illuminated by a laser for visual alignment and monitoring, and by an LED (M660L4, Thorlabs) for spectroscopic analysis, with manual and automated control implemented through a LabVIEW interface.

Droplet radius was determined spectroscopically from the backscattered Mie-resonance spectrum under LED illumination. The backscattered spectrum was recorded using a fiber-coupled spectrometer (Ocean Optics HR4000+), and resonance peak positions were fit using Mie theory (with a low-order Cauchy dispersion for the real refractive index) to retrieve droplet radius and the real refractive index.

The RH in the EDB chamber was controlled by mixing humidified and dry N_2 at a fixed total flow (200 sccm). The humidified stream was generated using a temperature-controlled water bath housed in the reservoir of a recirculating chiller, which also regulated the chamber temperature. The chamber and water bath were held below ambient temperature to reduce condensation in the delivery tubing. RH was changed

Table 2 Effective oscillator parameters of best fit (with 95% confidence intervals) for the model prebiotic seawater solutions studied here, together with parameters from the power-law hygroscopic growth fit $rGF(a_w) = \alpha(1 - a_w)^{-\gamma}$ and the efflorescence relative humidity (ERH)

Solution	$\tilde{B}$ (μm^{-1})	$\tilde{\nu}_0$ (μm^{-1})	$\tilde{\Gamma}$ (μm^{-1})	α	γ	ERH (%)
SW1	8.403 ± 0.055	8.061 ± 0.047	$(9.2 \pm 1.5) \times 10^{-7}$	1.38859 ± 0.00057	0.23626 ± 0.00032	41 ± 1%
SW2	9.476 ± 0.050	8.349 ± 0.039	$(1.28 \pm 0.30) \times 10^{-6}$	1.4245 ± 0.0011	0.21986 ± 0.00058	28 ± 1%
SW3	8.164 ± 0.052	7.849 ± 0.045	$(6.9 \pm 1.7) \times 10^{-7}$	1.39364 ± 0.00082	0.23503 ± 0.00046	41 ± 1%
MSW	8.753 ± 0.047	8.409 ± 0.041	$(9.6 \pm 1.7) \times 10^{-7}$	1.37422 ± 0.00096	0.23699 ± 0.00052	40 ± 1%

in a pseudo-continuous mode using small RH changes on short time intervals, allowing rapid acquisition of complete growth curves when needed. Measurements were performed in dual-droplet mode, in which a co-levitated probe droplet (*e.g.* NaCl at RH >50% or LiCl at RH >10%) is used to infer the chamber RH from its measured radial growth factor *via* established parameterizations, with an accuracy of much better than 1%.[51] Hygroscopic growth of the sample is reported as the radial growth factor,

$$\mathrm{rGF}(a_w) = \frac{r(a_w)}{r_{dry}}, \quad (3)$$

where $r(a_w)$ is the equilibrium droplet radius at water activity a_w and r_{dry} is the corresponding dry particle radius. As with the optical trapping experiments, measurements are performed on micron-sized droplets. Therefore, the Kelvin effect is neglected and $a_w \approx$ RH/100%. The RH was decreased toward the lowest accessible water activities (approaching efflorescence for salts) and then increased to check for hysteresis, yielding equilibrium growth curves as a function of water activity.

For comparison across compositions, the measured growth curves were additionally parameterized using a two-parameter power-law form,[52,53]

$$\mathrm{rGF}(a_w) = \alpha(1 - a_w)^{-\gamma}, \quad (4)$$

where α and γ are parameters of best-fit. The fit was performed by linearizing the expression as $\ln(\mathrm{rGF}) = \ln(\alpha) - \gamma \ln(1 - a_w)$ and applying least-squares regression over the measured water activity range.

The solute and water volume fractions used in the effective oscillator mixing expressions were obtained from the measured hygroscopic growth. For a droplet with dry radius r_{dry} and equilibrium radius $r(a_w) = r_{dry}\mathrm{rGF}(a_w)$, we assume that the dry-particle volume corresponds to the (nonvolatile) solute volume and that volumes are additive upon hydration. The solute volume fraction is then $\phi_s(a_w) = V_s/V = (r_{dry}/r)^3 = \mathrm{rGF}(a_w)^{-3}$, and the water volume fraction is $\phi_w(a_w) = 1 - \phi_s(a_w)$. In practice, $\mathrm{rGF}(a_w)$ is evaluated using the smooth power-law parameterization in eqn (4), yielding $\phi_s(a_w) = [\alpha(1-a_w)^{-\gamma}]^{-3}$ and $\phi_w(a_w) = 1 - \phi_s(a_w)$ at the water activities required for the optical-property analysis.

3 Results and discussion

3.1 Prebiotic seawater analogs and hygroscopic growth

The exact composition of seawater during the Hadean eon is unknown. However, two common approaches are widely used to construct prebiotic seawater analogs for laboratory and modeling studies. First, sulfate concentrations in Precambrian seawater are thought to have been far lower than modern values, motivating solutions in which sulfate is removed and chloride serves as the dominant counterion while modern-like major-cation ratios are retained. Accordingly, SW1 and SW3 were prepared by replacing sulfate with chloride, following previous prebiotic seawater formulations.[14,39] Second, crust–water interaction experiments have been used to infer alternative ion ratios by reacting basaltic rocks with water at elevated temperature and pressure, producing solutions with substantially enhanced calcium relative to modern seawater.[16] SW2 was chosen to represent this Ca-enriched scenario. The ion mole fractions defining all three solutions are summarized in Table 1. Minor ions beyond Na^+, K^+, Mg^{2+}, Ca^{2+}, Cl^-, and SO_4^{2-} were neglected because they are not expected to measurably affect the refractive index within experimental uncertainty. Modern seawater (MSW) was included here as an inorganic baseline for comparison with the prebiotic analog solutions. Possible effects of organic constituents, which can be important in present-day marine aerosol, were not considered in this work.

EDB measurements were performed to determine the hygroscopicity of the three prebiotic seawater compositions (SW1–SW3), with MSW included as a present-day benchmark. The radial growth factor, $\mathrm{rGF}(a_w)$, is shown in Fig. 2. The points represent measured growth factors and the lines show the smooth power-law parameterization in eqn (4), with fitted parameters reported in Table 2. Measurements extend to water activities approaching the efflorescence relative humidity (ERH). SW1, SW3, and modern seawater (MSW) exhibit ERH values in the 40–45% range, consistent with NaCl-dominated mixtures,[54] whereas SW2 effloresces at lower water activity due to the high hygroscopicity of calcium chloride and the absence of sulfate (preventing formation of $CaSO_4 \cdot H_2O$, which would otherwise raise the ERH to ~65–68% (ref. 55)).

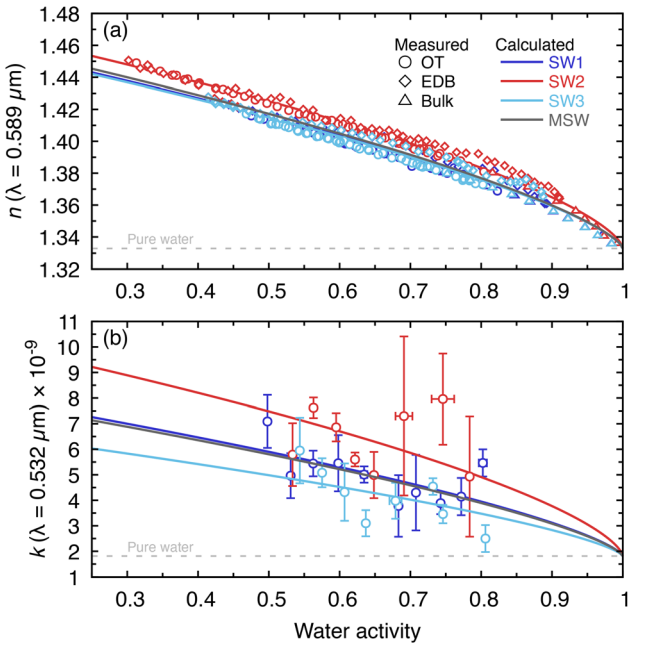

Fig. 3 (a) Real part of the refractive index, *n*, at 0.589 μm and (b) imaginary part of the refractive index, *k*, at 0.532 μm as a function of water activity for SW1–SW3 and modern seawater (MSW). Circles represent OT (Raman-based) measurements, diamonds represent EDB (elastic-scattering) measurements, and triangles represent bulk refractometer measurements; solid lines show the effective oscillator model calculations. Grey dashed lines indicate the refractive index of pure water at the corresponding wavelength (*n* from Harvey *et al.*[48] and *k* from Segelstein[49]).

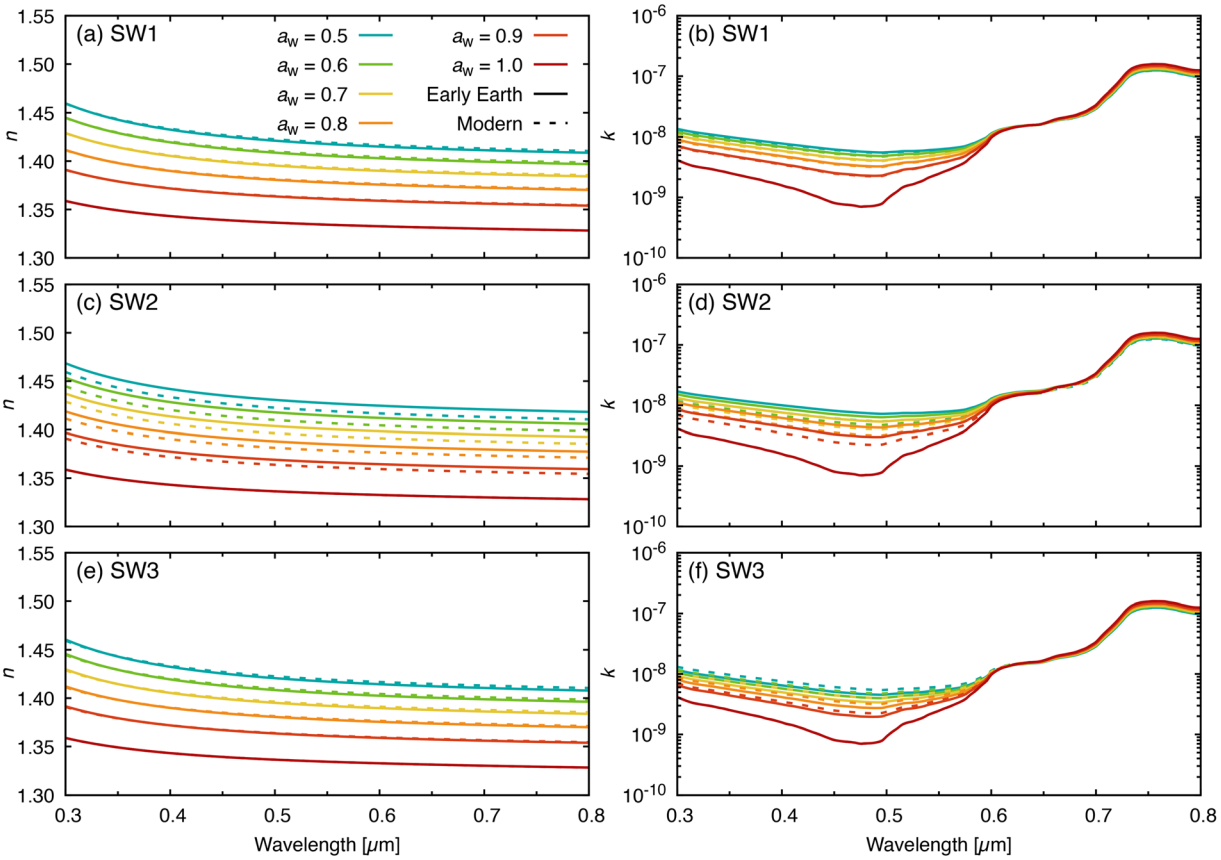

Fig. 4 Wavelength-dependent real (n) and imaginary (k) parts of the refractive index for (a and b) SW1, (c and d) SW2, and (e and f) SW3 at water activities, a_w, of 0.5, 0.6, 0.7, 0.8, 0.9, and 1.0. Solid lines represent prebiotic seawater (Early Earth) and dashed lines represent modern seawater (MSW) for comparison.

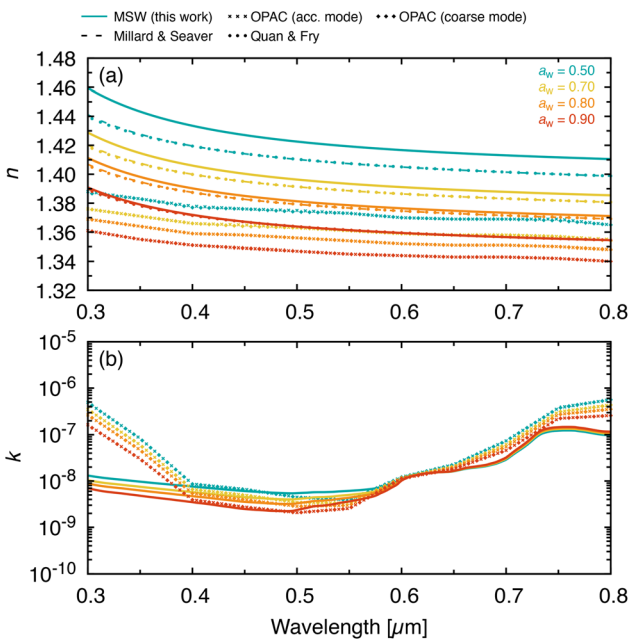

Fig. 5 Comparison of the wavelength-dependent (a) real and (b) imaginary parts of the refractive index for MSW (this work, solid lines) with literature values from Millard and Seaver,[32] Quan and Fry,[33] and the OPAC database[9,10] at water activities, a_w, of 0.5, 0.7, 0.8, 0.9, and 1.0.

Despite differences in efflorescence behavior, the three prebiotic solutions exhibit similar growth factors across the measured range and show only weak composition dependence. Hygroscopicity measurements for modern sea salt reported by previous work fall within the range spanned by the three solutions,[54–56] and our MSW measurements are likewise comparable.

3.2 Refractive index at single visible wavelengths

In the context of early Earth, these optical-property measurements are relevant both for radiative-transfer constraints on ocean–atmosphere light propagation and for the optical representation of seawater-derived marine aerosol particles. For all systems, MDR fits to OT Raman spectra and EDB elastic light scattering spectra were used to retrieve the wavelength-dependent real part of the refractive index (n), while the imaginary part of the refractive index (k) was determined only at the trapping laser wavelength (532 nm) using the method described in ref. 47. The effective oscillator model[47] provides a compact representation of the measurements and enables interpolation across water activity and wavelength.

Measurements of n at 589 nm (sodium D-line) are shown in Fig. 3a as a function of water activity over the range a_w = 0.25–1.0. This wavelength was chosen for n because it corresponds to

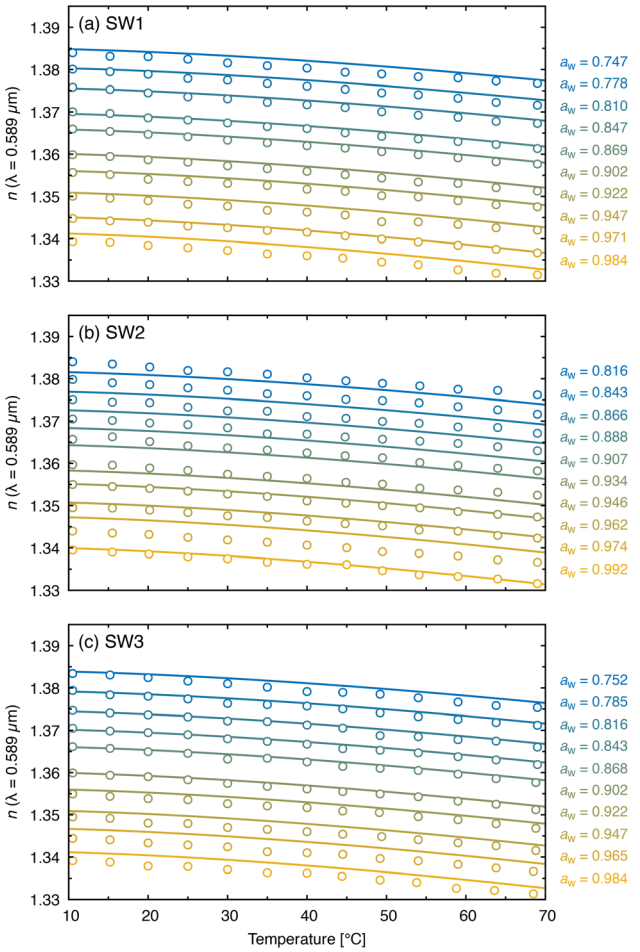

Fig. 6 Temperature dependence of the real refractive index, $n(\lambda = 589$ nm), for the model prebiotic seawater solutions (a) SW1, (b) SW2, and (c) SW3. Open circles show bulk refractometer measurements at the water activities a_w listed in the legend (colors correspond to a_w). Solid curves are best-fit effective-oscillator-model results, capturing the systematic decrease in n with increasing temperature over 10–70 °C.

the measurement wavelength of the bulk refractometer, enabling direct comparison between the single-particle datasets (OT and EDB) and the bulk refractometer dataset, all of which are shown. At high water activity (dilute solutions), n for all solutions approaches that of pure water ($n \approx 1.333$ at 589 nm).[57] As water activity decreases and solute concentration increases, n rises monotonically, reaching ~1.45–1.50 near the lowest accessible water activities. SW1 and SW3, which share similar ion mole fractions (Table 1), exhibit nearly identical $n(a_w)$ curves across the full range and track MSW closely. SW2, which has substantially higher $CaCl_2$ content, shows a modestly elevated refractive index at intermediate and low water activities, consistent with the greater density and polarizability of Ca-rich brines.

The effective oscillator model reproduces the measured $n(a_w)$ trends well (Fig. 3a). To further validate the single-particle measurements, bulk refractometer measurements were also conducted between $a_w \approx 0.80$ (near the bulk solubility limit) and $a_w \approx 0.99$. The measured n values agree closely with both the single-particle results and the model calculations, supporting internal consistency between the two measurement approaches.

The imaginary part of the refractive index, k, is shown in Fig. 3b. In practice, the accessible range for k measurements is restricted to $a_w \gtrsim 0.50$, because droplets frequently crystallize when exposed to increased laser power at lower water activities, consistent with reports of non-photochemical laser-induced nucleation in supersaturated solutions.[58] Across the measured range, k(532 nm) is extremely small (on the order of 10^{-9}–10^{-8}) and approaches the pure-water value as the solutions become increasingly dilute. The very small magnitudes of k indicate that these inorganic prebiotic seawater analogs are effectively transparent at visible wavelengths, implying that their solar-wavelength radiative effects (including those of marine aerosol particles derived from these solutions) are dominated by scattering in the absence of dissolved chromophores.

3.3 Wavelength dependence and comparison to existing optical constants

Fig. 4 shows the calculated wavelength-dependent complex refractive index for the three model prebiotic solutions together with MSW, across representative water activities. The effective oscillator model[47] was used to extend the experimental constraints to wavelengths beyond those directly measured and to provide a continuous parameterization in a_w. SW1 and SW3 agree closely with MSW across the wavelength range, consistent with their similar major-ion distributions (Table 1). SW2 exhibits the largest deviations from MSW, particularly in concentrated regimes where composition differences exert a larger influence on dispersion. These wavelength-dependent refractive index data are needed for radiative-transfer and scattering calculations representing seawater-derived marine aerosols interacting with solar radiation across the spectrum.

Fig. 5 compares the calculated wavelength-dependent refractive index for MSW with literature values from Millard and Seaver, Quan and Fry, and with the Optical Properties of Aerosols and Clouds (OPAC) database representation for marine aerosol.[9,10,32,33] For the real part, both the OPAC accumulation-mode and coarse-mode values are systematically lower than our results across all water activities and wavelengths. This underestimation likely stems from the use of volume mixing rules in OPAC to calculate water activity-dependent refractive index values from those of pure water and sea salt,[9,59] thereby neglecting non-ideal interactions. Discrepancies between model parameterizations and measured sea spray refractive indices have been noted previously,[60] and inaccurate representations of n may introduce substantial errors in aerosol optical depth and radiative forcing calculations.[61,62]

In contrast, application of the hygroscopicity measurements to the Millard and Seaver[32] and Quan and Fry[33] parameterizations agrees closely with our measurements at water activities typical of humid marine boundary-layer conditions ($a_w \gtrsim 0.8$), while differences become more apparent at lower water activity, where solutions are more concentrated. This is not surprising,

as these lower water activities lie outside the range of the datasets used to create those parameterizations, which extend only to a salinity of 43 psu ($a_w \approx 0.98$) and require substantial extrapolation of the parameterizations. In fact, given the magnitude of this extrapolation, the level of agreement observed down to low a_w is remarkable and, in part, can be attributed to the proper treatment of non-ideal mixing. For the imaginary part, our values remain very small in the visible and are broadly consistent with water-dominated absorption and with the OPAC tabulation (the parameterizations[32,33] do not include k). Larger discrepancies outside the visible are expected because different datasets and parameterizations are used to represent water absorption and dispersion in these compilations.

3.4 Temperature dependence of n

Bulk refractometer measurements allow determination of the temperature dependence of n at 589 nm for solute concentrations below the bulk solubility limit (Fig. 6). Across all water activities and solutions, increasing temperature decreases n, consistent with reduced solution density. Within the effective oscillator framework, the temperature dependence of n enters through the pure-water contribution $n^{(w)}(\nu, T)$, which is evaluated using the Harvey *et al.* parameterization[48] at the temperature of interest. The solute oscillator parameters $\tilde{B}$ and $\tilde{\nu}_0$ are approximated as temperature-independent, so the temperature variation of n for the solution is governed by the well-characterized temperature dependence of the water refractive index.

In Fig. 6, model curves calculated in this way reproduce the measured temperature slopes well across the full range examined. These temperature-dependent data enable refractive indices for seawater and seawater-derived marine aerosols to be estimated under a broader range of early Earth surface conditions rather than relying on room-temperature values alone.

Fig. 7 combines the temperature and wavelength dependence of n for MSW and compares the results with literature parameterizations from Millard and Seaver[32] and Quan and Fry[33] at four wavelengths (0.4, 0.5, 0.6, and 0.7 μm) over 0–40 °C. At all wavelengths and water activities examined, the effective oscillator model reproduces the observed decrease in n with increasing temperature. The Millard and Seaver parameterization agrees well with our results at high water activity, where both datasets are constrained by direct measurements. At lower

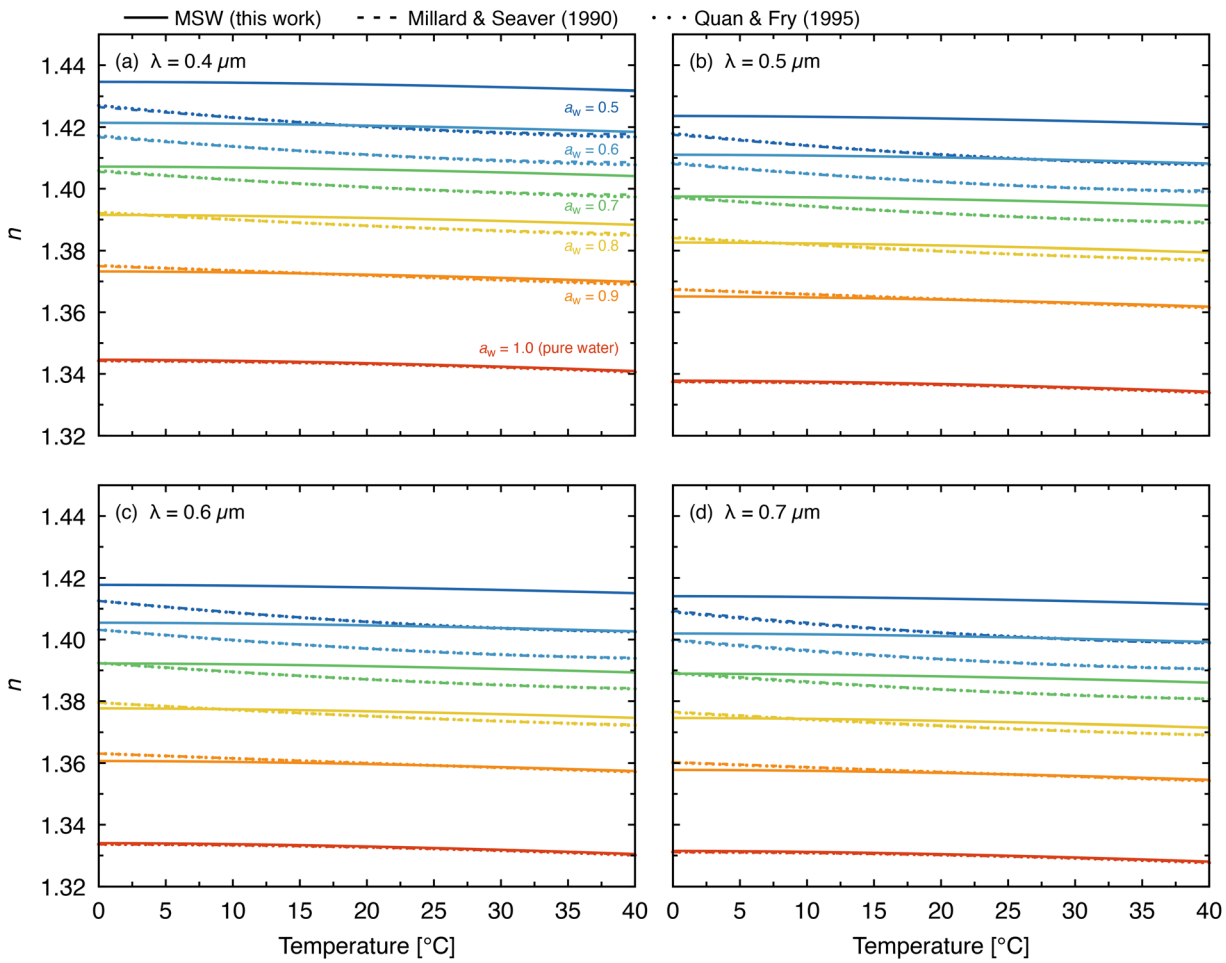

Fig. 7 Temperature dependence of the real refractive index for MSW at various water activities compared to the parameterizations of Millard and Seaver[32] and Quan and Fry[33] at (a) 0.4 μm, (b) 0.5 μm, (c) 0.6 μm, and (d) 0.7 μm. Solid lines show MSW from this work, dashed lines show Millard and Seaver, and dotted lines show Quan and Fry. Colors correspond to water activity, a_w. Temperature range is 0–40 °C.

a_w, deviations grow as the Millard and Seaver parameterization is extrapolated well beyond its original salinity range, consistent with the comparison at room temperature (Fig. 5). The Quan and Fry parameterization shows nearly identical deviations at lower water activities. Together, the wavelength- and temperature-dependent parameterization reported here provides a self-consistent description of the complex refractive index of prebiotic and modern seawater analogs over the ranges of wavelength (0.3–0.8 μm), water activity (0.25–1.0), and temperature (10–70 °C) relevant to early Earth radiative-transfer and photochemical calculations.

4 Conclusions

We report wavelength-, temperature-, and water-activity-dependent complex refractive indices for three model prebiotic seawater solutions and modern seawater, combining single-particle measurements (OT and EDB) with bulk refractometry. Although the aerosol particles studied here were generated by nebulization or piezoelectric droplet generation rather than by bubble bursting, the consistency between the OT, EDB, and bulk measurements supports their use as model seawater-derived aerosol analogs for these simplified inorganic solutions. The two sulfate-depleted, chloride-dominated solutions (SW1 and SW3) track modern seawater closely across all conditions, while the Ca-enriched solution (SW2) shows modestly higher n at intermediate and low a_w, as well as the largest departures from modern seawater dispersion. For all compositions, k is on the order of 10^{-9} in the visible, indicating very weak absorption in the absence of dissolved chromophores. Accordingly, the single-scattering albedo at visible wavelengths is expected to be very close to unity for representative particle sizes. Comparison with existing compilations reveals poor agreement with the OPAC database for the real refractive index of marine aerosol, while commonly used parameterizations[32,33] agree well at high a_w but deviate where extrapolation beyond their original salinity range is required. EDB measurements confirm similar hygroscopic growth across the three analog solutions, supporting their use as controlled proxies for seawater-derived aerosol.

The effective oscillator model provides a compact, Kramers–Kronig-consistent parameterization of n and k over the ranges of wavelength (0.3–0.8 μm), water activity (0.25–1.0), and temperature (10–70 °C) relevant to early Earth radiative-transfer and photochemical calculations, and offers physically grounded inputs for representing the optical impacts of marine aerosols generated from hypothesized prebiotic seawater.

Conflicts of interest

There are no conflicts to declare.

Data availability

The processed refractive-index datasets are available from the corresponding author upon reasonable request. The MATLAB code implementing all functions used in this work is provided in the supplementary information (SI) with a README, together with scripts that reproduce the calculations and figures reported in the manuscript. Supplementary information: MATLAB files implementing the effective oscillator model to generate the calculated wavelength-dependent complex refractive index results, together with a README describing usage and required inputs. See DOI: https://doi.org/10.1039/d6ea00030d.

Acknowledgements

This work is supported by the Alfred P. Sloan Foundation (Grant Number: G-2024-22579).

References

1 T. M. Harrison, *Hadean Earth*, Springer, 2020.
2 A. A. Novoselov, D. Silva, J. Schneider, X. C. Abrevaya, M. S. Chaffin, P. Serrano, M. S. Navarro, M. J. Conti and C. R. d. Souza Filho, Geochemical constraints on the hadean environment from mineral fingerprints of prokaryotes, *Sci. Rep.*, 2017, **7**, 4008.
3 C. Sagan and G. Mullen, Earth and mars: Evolution of atmospheres and surface temperatures, *Science*, 1972, **177**, 52–56.
4 G. Feulner, The faint young sun problem, *Rev. Geophys.*, 2012, **50**, RG2006.
5 S. Ranjan, C. L. Kufner, G. G. Lozano, Z. R. Todd, A. Haseki and D. D. Sasselov, UV transmission in natural waters on prebiotic earth, *Astrobiology*, 2022, **22**, 242–262.
6 E. R. Lewis and S. E. Schwartz, Sea Salt Aerosol Production: Mechanisms, Methods, Measurements, and Models, *Geophysical Monograph Series*, American Geophysical Union, 2004, vol. 152.
7 C. D. O'Dowd and G. De Leeuw, Marine aerosol production: a review of the current knowledge, *Philos. Trans. R. Soc., A*, 2007, **365**, 1753–1774.
8 P. K. Quinn, D. B. Collins, V. H. Grassian, K. A. Prather and T. S. Bates, Chemistry and related properties of freshly emitted sea spray aerosol, *Chem. Rev.*, 2015, **115**, 4383–4399.
9 M. Hess, P. Koepke and I. Schult, Optical properties of aerosols and clouds: The software package opac, *Bull. Am. Meteorol. Soc.*, 1998, **79**, 831–844.
10 OPAC (Optical Properties of Aerosols and Clouds) aerosol database. GEISA (AERIS) portal. URL https://geisa.aeris-data.fr/opac/, Accessed 2026-02-10.
11 D. E. Canfield, K. S. Habicht and B. Thamdrup, The archean sulfur cycle and the early history of atmospheric oxygen, *Science*, 2000, **288**, 658–661.
12 S. A. Crowe, G. Paris, S. Katsev, C. Jones, S.-T. Kim, A. L. Zerkle, S. Nomosatryo, D. A. Fowle, J. F. Adkins, A. L. Sessions, *et al.*, Sulfate was a trace constituent of archean seawater, *Science*, 2014, **346**, 735–739.
13 T. W. Lyons, C. T. Reinhard and N. J. Planavsky, The rise of oxygen in earth's early ocean and atmosphere, *Nature*, 2014, **506**, 307–315.

14 R. Tostevin and I. A. Ahmed, Micronutrient availability in precambrian oceans controlled by greenalite formation, *Nat. Geosci.*, 2023, **16**, 1188–1193.
15 D. C. Catling and K. J. Zahnle, The archean atmosphere, *Sci. Adv.*, 2020, **6**, eaax1420.
16 H. Ueda and T. Shibuya, Composition of the primordial ocean just after its formation: constraints from the reactions between the primitive crust and a strongly acidic, co2-rich fluid at elevated temperatures and pressures, *Minerals*, 2021, **11**, 389.
17 L. P. Knauth, Salinity history of the earth's early ocean, *Nature*, 1998, **395**, 554–555.
18 B. Marty, G. Avice, D. V. Bekaert and M. W. Broadley, Salinity of the archaean oceans from analysis of fluid inclusions in quartz, *C. R. Geosci.*, 2018, **350**, 154–163.
19 D. D. Channer, C. De Ronde and E. Spooner, The cl- br- i-composition of 3.23 ga modified seawater: implications for the geological evolution of ocean halide chemistry, *Earth Planet. Sci. Lett.*, 1997, **150**, 325–335.
20 J. Foriel, P. Philippot, P. Rey, A. Somogyi, D. Banks and B. Ménez, Biological control of Cl/Br and low sulfate concentration in a 3.5-Gyr-old seawater from North Pole, Western Australia, *Earth Planet. Sci. Lett.*, 2004, **228**, 451–463.
21 K. Farber, A. Dziggel, F. M. Meyer, W. Prochaska, A. Hofmann and C. Harris, Fluid inclusion analysis of silicified palaeoarchaean oceanic crust–a record of archaean seawater?, *Precambrian Res.*, 2015, **266**, 150–164.
22 C. E. J. De Ronde, D. M. d. Channer, K. Faure, C. J. Bray and E. T. C. Spooner, Fluid chemistry of Archean seafloor hydrothermal vents: Implications for the composition of circa 3.2 ga seawater, *Geochim. Cosmochim. Acta*, 1997, **61**, 4025–4042.
23 B. W. Alexander, M. Bau, P. Andersson and P. Dulski, Continentally-derived solutes in shallow archean seawater: rare earth element and nd isotope evidence in iron formation from the 2.9 ga pongola supergroup, south africa, *Geochim. Cosmochim. Acta*, 2008, **72**, 378–394.
24 A. C. Khelen, C. Manikyamba, K. Subramanyam, M. Santosh, S. Ganguly, M. Kalpana and D. S. Rao, Archean seawater composition and depositional environment–geochemical and isotopic signatures from the stromatolitic carbonates of dharwar craton, india, *Precambrian Res.*, 2019, **330**, 35–57.
25 N. J. Tosca and B. M. Tutolo, Hydrothermal vent fluid-seawater mixing and the origins of archean iron formation, *Geochim. Cosmochim. Acta*, 2023, **352**, 51–68.
26 T. Komiya, T. Hirata, K. Kitajima, S. Yamamoto, T. Shibuya, Y. Sawaki, T. Ishikawa, D. Shu, Y. Li and J. Han, Evolution of the composition of seawater through geologic time, and its influence on the evolution of life, *Gondwana Res.*, 2008, **14**, 159–174.
27 F. Albarede, F. Thibon, J. Blichert-Toft and H. Tsikos, Chemical archeoceanography, *Chem. Geol.*, 2020, **548**, 119625.
28 C. L. Blättler, M. W. Claire, A. R. Prave, K. Kirsimäe, J. A. Higgins, P. V. Medvedev, A. E. Romashkin, D. V. Rychanchik, A. L. Zerkle, K. Paiste, *et al.*, Two-billion-year-old evaporites capture earth's great oxidation, *Science*, 2018, **360**, 320–323.
29 I. Halevy and A. Bachan, The geologic history of seawater ph, *Science*, 2017, **355**, 1069–1071.
30 S. Olson, M. F. Jansen, D. S. Abbot, I. Halevy and C. Goldblatt, The effect of ocean salinity on climate and its implications for earth's habitability, *Geophys. Res. Lett.*, 2022, **49**, e2021GL095748.
31 G. W. Ferreira, R. B. Samulewski, F. F. Ivashita, A. Paesano Jr, A. Urbano and D. A. M. Zaia, Did salts in seawater play an important role in the adsorption of molecules on minerals in the prebiotic earth? the case of the adsorption of thiocyanate onto forsterite-91, *Origins Life Evol. Biospheres*, 2023, **53**, 127–156.
32 R. C. Millard and G. Seaver, An index of refraction algorithm for seawater over temperature, pressure, salinity, density, and wavelength, *Deep-Sea Res., Part A*, 1990, **37**, 1909–1926.
33 X. Quan and E. S. Fry, Empirical equation for the index of refraction of seawater, *Appl. Opt.*, 1995, **34**, 3477–3480.
34 R. W. Austin and G. Halikas, *The Index of Refraction of Seawater*, Tech. Rep., Scripps Institution of Oceanography, University of California, San Diego and University of California, Los Angeles, San Diego, CA, USA and Los Angeles, CA, USA, 1976.
35 E. Stanley, The refractive index of seawater as a function of temperature, pressure and two wavelengths, *Deep-Sea Res. Oceanogr. Abstr.*, 1971, **18**, 833–840). URL https://www.sciencedirect.com/science/article/pii/0011747171900507.
36 J. Leyendekkers, Prediction of the refractive index of seawater as a function of temperature, pressure, salinity and wavelength, *Mar. Chem.*, 1977, **5**, 29–42.
37 A. Mehu and A. Johannin-Gilles, Variation de la réfraction spécifique de l'eau de mer étalon de copenhague et de ses dilutions en fonction de la longuerr d'onde, de la température et de la chlorinité, *Deep-Sea Res. Oceanogr. Abstr.*, 1969, **16**, 605–611). URL https://www.sciencedirect.com/science/article/pii/0011747169900618.
38 R. M. Pope and E. S. Fry, Absorption spectrum (380–700 nm) of pure water. ii. integrating cavity measurements, *Appl. Opt.*, 1997, **36**, 8710–8723.
39 K. Yusenko, S. Fox, P. Guni and H. Strasdeit, Model studies on the formation and reactions of solid glycine complexes at the coasts of a primordial salty ocean, *Z. Anorg. Allg. Chem.*, 2008, **634**, 2347–2354.
40 D. L. Pinti, The origin and evolution of the oceans, in *Lectures in Astrobiology*, Springer, 2005, vol. I,pp. 83–112.
41 J. L. Bischoff and F. W. Dickson, Seawater-basalt interaction at 200 c and 500 bars: implications for origin of sea-floor heavy-metal deposits and regulation of seawater chemistry, *Earth Planet. Sci. Lett.*, 1975, **25**, 385–397.
42 ASTM International, West Conshohocken, PA, USA, Standard Practice for the Preparation of Substitute Ocean Water (2003), Reapproved 2003; approved Aug. 10, 2003; published Sep. 2003.

43 A. Rafferty and T. C. Preston, Measuring the size and complex refractive index of an aqueous aerosol particle using electromagnetic heating and cavity-enhanced Raman scattering, *Phys. Chem. Chem. Phys.*, 2018, **20**, 17038–17047.
44 A. Logozzo and T. C. Preston, Temperature-controlled dual-beam optical trap for single particle studies of organic aerosol, *J. Phys. Chem. A*, 2022, **126**, 109–118.
45 T. C. Preston and J. P. Reid, Accurate and efficient determination of the radius, refractive index, and dispersion of weakly absorbing spherical particle using whispering gallery modes, *J. Opt. Soc. Am. B*, 2013, **30**, 2113–2122.
46 T. C. Preston and J. P. Reid, Determining the size and refractive index of microspheres using the mode assignments from mie resonances, *J. Opt. Soc. Am. A*, 2015, **32**, 2210–2217.
47 A. Bain and T. C. Preston, The wavelength-dependent optical properties of weakly absorbing aqueous aerosol particles, *Chem. Commun.*, 2020, **56**, 8928–8931.
48 A. H. Harvey, J. S. Gallagher and J. M. H. L. Sengers, Revised formulation for the refractive index of water and steam as a function of wavelength, temperature and density, *J. Phys. Chem. Ref. Data*, 1998, **27**, 761–774.
49 D. J. Segelstein, *The Complex Refractive Index of Water*, Master's thesis, University of Missouri, Kansas City, 1981.
50 L. P. Knauth, Temperature and salinity history of the Precambrian ocean: implications for the course of microbial evolution, in *Geobiology: Objectives, Concepts, Perspectives*, ed. Noffke, N., Elsevier B.V., Amsterdam, 2005, pp. 53–69.
51 J. M. Choczynski, R. Kaur Kohli, C. S. Sheldon, C. L. Price and J. F. Davies, A dual-droplet approach for measuring the hygroscopicity of aqueous aerosol, *Atmos. Meas. Tech.*, 2021, **14**, 5001–5013.
52 A. D. Clarke, S. Howell, P. K. Quinn, T. S. Bates, J. A. Ogren, E. Andrews, A. Jefferson, A. Massling, O. Mayol-Bracero, H. Maring, *et al.*, Indoex aerosol: A comparison and summary of chemical, microphysical, and optical properties observed from land, ship, and aircraft, *J. Geophys. Res.: Atmos.*, 2002, **107**(D19), 8033.
53 P. Zieger, E. Weingartner, J. Henzing, M. Moerman, G. De Leeuw, J. Mikkilä, M. Ehn, T. Petäjä, K. Clémer, M. Van Roozendael, *et al.*, Comparison of ambient aerosol extinction coefficients obtained from in-situ, max-doas and lidar measurements at cabauw, *Atmos. Chem. Phys.*, 2011, **11**, 2603–2624.
54 I. N. Tang, A. C. Tridico and K. H. Fung, Thermodynamic and optical properties of sea salt aerosols, *J. Geophys. Res.: Atmos.*, 1997, **102**, 23269–23275.
55 O. Reich, M. J. Gleichweit, G. David, N. Leemann and R. Signorell, Hygroscopic growth of single atmospheric sea salt aerosol particles from mass measurement in an optical trap, *Environ. Sci.: Atmos.*, 2023, **3**, 695–707.
56 P. Zieger, O. Väisänen, J. C. Corbin, D. G. Partridge, S. Bastelberger, M. Mousavi-Fard, B. Rosati, M. Gysel, U. K. Krieger, C. Leck, *et al.*, Revising the hygroscopicity of inorganic sea salt particles, *Nat. Commun.*, 2017, **8**, 15883.
57 M. Daimon and A. Masumura, Measurement of the refractive index of distilled water from the near-infrared region to the ultraviolet region, *Appl. Opt.*, 2007, **46**, 3811–3820.
58 B. A. Garetz, J. E. Aber, N. L. Goddard, R. G. Young and A. S. Myerson, Nonphotochemical, polarization-dependent, laser-induced nucleation in supersaturated aqueous urea solutions, *Phys. Rev. Lett.*, 1996, **77**, 3475–3476.
59 E. P. Shettle and R. W. Fenn, *Models for the Aerosols of the Lower Atmosphere and the Effects of Humidity Variations on Their Optical Properties*, Tech. Rep. AFGL-TR-79-0214, Air Force Geophysics Laboratory, Hanscom AFB, MA, USA, 1979.
60 C. Fan, B. He, S. Guo, J. Qiu and C. Zhao, Insights into the real part of natural sea spray aerosol refractive index in the pacific ocean, *Atmos. Chem. Phys.*, 2025, **25**, 5761–5771.
61 C. Erlick, J. P. Abbatt and Y. Rudich, How different calculations of the refractive index affect estimates of the radiative forcing efficiency of ammonium sulfate aerosols, *J. Atmos. Sci.*, 2011, **68**, 1845–1852.
62 A. M. Aldhaif, C. Stahl, R. A. Braun, M. A. Moghaddam, T. Shingler, E. Crosbie, P. Sawamura, H. Dadashazar, L. Ziemba, J. L. Jimenez, *et al.*, Characterization of the real part of dry aerosol refractive index over north america from the surface to 12 km, *J. Geophys. Res.: Atmos.*, 2018, **123**, 8283–8300.